

## Far-reaching effects of tyrosine64 phosphorylation on Ras revealed with $\text{BeF}_3^-$ complexes

Patrick Baumann <sup>1,2,3</sup> & Yi Jin <sup>1,2,3</sup> 

Tyrosine phosphorylation on Ras by Src kinase is known to uncouple Ras from upstream regulation and downstream communication. However, the mechanisms by which phosphorylation modulates these interactions have not been detailed. Here, the major monophosphorylation level on tyrosine64 is quantified by  $^{31}\text{P}$  NMR and mutagenesis. Crystal structures of unphosphorylated and tyrosine64-phosphorylated Ras in complex with a  $\text{BeF}_3^-$  ground state analogue reveal “closed” Ras conformations very different from those of the “open” conformations previously observed for non-hydrolysable GTP analogue structures of Ras. They deliver new mechanistic and conformational insights into intrinsic GTP hydrolysis. Phosphorylation of tyrosine64 delivers conformational changes distant from the active site, showing why phosphorylated Ras has reduced affinity to its downstream effector Raf.  $^{19}\text{F}$  NMR provides evidence for changes in the intrinsic GTPase and nucleotide exchange rate and identifies the concurrent presence of a major “closed” conformation alongside a minor yet functionally important “open” conformation at the ground state of Ras. This study expands the application of metal fluoride complexes in revealing major and minor conformational changes of dynamic and modified Ras proteins.

<sup>1</sup>School of Chemistry, Cardiff University, Park Place, Cardiff CF10 3AT, UK. <sup>2</sup>Department of Chemistry, School of Natural Sciences, Faculty of Science and Engineering, University of Manchester, M13 9PL, Manchester, UK. <sup>3</sup>Present address: Manchester Institute of Biotechnology, University of Manchester, 131 Princess Street, Manchester M1 7DN, UK. ✉email: [yi.jin@manchester.ac.uk](mailto:yi.jin@manchester.ac.uk)

The three human oncogenes, HRas, NRas and KRas, encode highly related membrane-bound Ras protein isoforms that act as “molecular switches” cycling between GDP-bound and GTP-bound forms<sup>1,2</sup>. Guanine nucleotide-exchange factors (GEFs) are recruited to promote the intrinsically slow GDP to GTP nucleotide exchange, which is coupled to distinct conformations at Switch I (residues 30–38) and Switch II (residues 59–72) near GDP/GTP binding site<sup>3</sup>. The GTP-bound active form has a high affinity to downstream effector proteins, such as Raf, and triggers the mitogen-activated protein kinase (MAPK) pathway<sup>3</sup>. This GTPase signalling is terminated by accelerated GTP hydrolysis catalysed by GTPase-activating proteins (GAPs)<sup>4</sup>. Deregulation of the GTPase cycle in Ras is commonly associated with cancer initiation and progression<sup>5</sup>.

Protein tyrosine kinase Src was recently shown to phosphorylate Ras proteins on tyrosine residues 32 and 64<sup>6,7</sup>. It was first reported that Src predominantly phosphorylates Y32 in the GDP-bound GST-tagged Ras and was thought to allow the more favoured displacement of downstream effector Raf by GAP, which then increases GAP-catalysed GTP hydrolysis<sup>6,8</sup>. That led to a focused investigation<sup>8</sup> on the effect of SHP2-mediated dephosphorylation, only on Y32. However, it was later found that Ras in both GDP and GTP-bound forms can be phosphorylated on Y64 in Switch II faster than Y32 in Switch I by Src which reduces the activity of GAP<sup>7</sup>. Therefore, phosphorylation of these sites has been proposed as the mechanism for uncoupling phosphorylated Ras from upstream regulation *in vivo*, especially by attenuation both of the nucleotide exchange catalysed by GEF and of GTP hydrolysis activity catalysed by GAP<sup>7</sup>. Particularly, Y64 has been identified as one of the major hotspots for effector interaction<sup>9</sup>. Nonetheless, contradictory findings regarding Src-mediated phosphorylation levels on Y32 and Y64 have given rise to divergent hypotheses. These hypotheses revolve around whether phosphorylation enhances or diminishes GAP binding, and subsequently, how this modulation influences GTP hydrolysis rate and downstream effector interactions<sup>6,7</sup>. To date, only a handful of computational investigations have centred on the conformational ramifications of mono-phosphorylation on Y32 or dual phosphorylation on both Y32 and Y64 concerning effector and inhibitor interactions<sup>10–12</sup>. Nonetheless, the accurate quantification of each tyrosine phosphorylation level and the specific ways in which phosphorylation influences intrinsic Ras nucleotide exchange, GTP hydrolysis, and interactions with downstream effectors all remain elusive<sup>7,13</sup>.

Pre-hydrolysis state structures of Ras provide conformational information for substrate binding and explain the molecular origin of intrinsic GTP hydrolysis and nucleotide exchange. They have been depicted by numerous structures of Ras co-crystallised with non-hydrolysable GTP analogues, including guanosine 5'-[ $\beta,\gamma$ -imido] triphosphate (GMPPNP), guanosine 5'-[ $\beta,\gamma$ -methylene] triphosphate (GMPPCP), and guanosine 5'-O-[ $\gamma$ -thio] triphosphate (GTP $\gamma$ S). However, because of their non-isopolar chemical changes<sup>14</sup>, these compounds have modified electron densities on their  $\gamma$ -phosphate oxygens resulting in changed protonation states in bound complexes for Ras and significantly modified H-bonding compared to the true ground state of GTP in Ras<sup>15,16</sup>. Metal fluoride complexes (MF<sub>x</sub>) have been used extensively in structural biology to monitor conformational changes and address the activation origin of proteins<sup>17</sup>. The ground state analogue (GSA) BeF<sub>3</sub><sup>-</sup> (Protein Data Bank (PDB) Chemical ID BEF) mimics the tetrahedral geometry of phosphate before or after phosphoryl transfer. <sup>19</sup>F NMR as a highly sensitive technique offers a more direct spectroscopic approach to provide a detailed picture of the charge distribution in the ground and transition states for P–O bond through MF<sub>x</sub> complexes mimicking the  $\gamma$ -phosphate of GTP in GTPases<sup>18,19</sup>,  $\gamma$ -phosphate

of ATP in kinases<sup>20,21</sup>, and bacterial phosphatases and phosphomutases<sup>22–27</sup>. <sup>19</sup>F NMR has also successfully reported the conformational changes that regulate the phosphatase activity of bacterial histidine kinase with BeF<sub>3</sub><sup>-</sup> complexes<sup>26,28</sup>. For Ras, GDP-BeF<sub>3</sub><sup>-</sup> could provide a valuable alternative ground state conformation because all three fluorine atoms are capable of accepting H-bonds as a fully deprotonated  $\gamma$ -phosphate in GTP<sup>15</sup>. However, no x-ray structures of the BeF<sub>3</sub><sup>-</sup> GSA complex for Ras have been deposited in the PDB to date.

We here show by mutagenesis and <sup>31</sup>P NMR the mono-phosphorylation level on Y64 in Ras is significantly higher than for other mono- and double-phosphorylated species, ruling out Src being a dual-kinase for Ras. Our work delivers pioneering BeF<sub>3</sub><sup>-</sup> GSA complex x-ray structures for unphosphorylated (Ras<sub>WT</sub>) and Y64-monophosphorylated Ras (Ras<sub>pY64</sub>) that unveil novel “closed” ground state conformations for the intrinsic hydrolysis of Ras, which are distinct from other non-hydrolysable GTP analogue-bound structures. The phosphorylation on Y64 in Switch II triggers a cascade of conformational changes beyond the active site, potentially impairing the binding of Ras to downstream effector Raf and offering an alternative mechanism to previous proposals<sup>12</sup>. Combined with high-resolution x-ray crystal structures, the subtle yet significant <sup>19</sup>F NMR chemical shifts and linewidth changes between Ras<sub>WT</sub>-GDP-BeF<sub>3</sub><sup>-</sup> and Ras<sub>pY64</sub>-GDP-BeF<sub>3</sub><sup>-</sup> GSA complexes offer viable insights into decreased intrinsic GTPase rate and increased nucleotide exchange rate on phosphorylation<sup>6</sup>. Our study expands the evidence-based understanding of post-translational modification (PTM)-induced conformational changes of Ras. Furthermore, it underscores the capability of <sup>19</sup>F NMR to detect unnoticed conformations and conformational alterations in high-resolution structures, demonstrated here *via* MF<sub>x</sub> complexes.

## Results and discussion

### Phosphorylation of Y64 is the main Ras site for Src kinase.

Expression tags have been shown to affect the site preference of tyrosine phosphorylation of Ras<sup>6</sup>. Thus, we recombinantly generated un-tagged Ras. A phosphorylation assay of the GDP-bound HRas (hereafter Ras) by Src catalytic domain was set up by using physiologically relevant concentrations of Mg<sup>2+</sup> and ATP<sup>29</sup>. Mass spectroscopy (MS) analysis detected unphosphorylated, mono-, and double-phosphorylated species (Supplementary Figure 1). To quantify the site-specific phosphorylation, ion exchange chromatography was used to separate major mono-phosphorylated Ras species from non- and double-phosphorylated ones; double-phosphorylated species only show minor peaks (Supplementary Figure 2). The sole mono-phosphorylated Ras fraction was trypsin digested and MS detected phosphorylated peptide fragments only on Y64 (Supplementary Figure 3). To specifically quantify phosphorylation levels, Y32F and Y64F variants of Ras, Ras<sub>Y32F</sub> and Ras<sub>Y64F</sub>, were also prepared and phosphorylated by Src under the same condition as for Ras<sub>WT</sub>. <sup>31</sup>P NMR shows the integration of the resonance from the phosphorylated tyrosine (–0.4 ppm) is reduced by 85% for the Ras<sub>Y64F</sub> variant compared to Ras<sub>WT</sub> and Ras<sub>Y32F</sub> variant (Fig. 1). This reveals that Y64 is the main phosphorylation target of Src. It conflicts with the conclusion in previous work that Y32 is the major phosphorylation site, possibly due to the *in vitro* phosphorylation assay was there carried out with GST-tagged HRas<sup>6</sup>. In addition, the resonance of P<sup>B</sup> 30 of the bound GDP in the Y64-phosphorylated Ras<sub>Y32F</sub> variant moved downfield by 0.5 ppm relative to the less-phosphorylated Ras<sub>Y64F</sub> variant, indicating the mutation of Y32 to F has induced local conformational changes around the P-loop (Fig. 1)<sup>31</sup>.

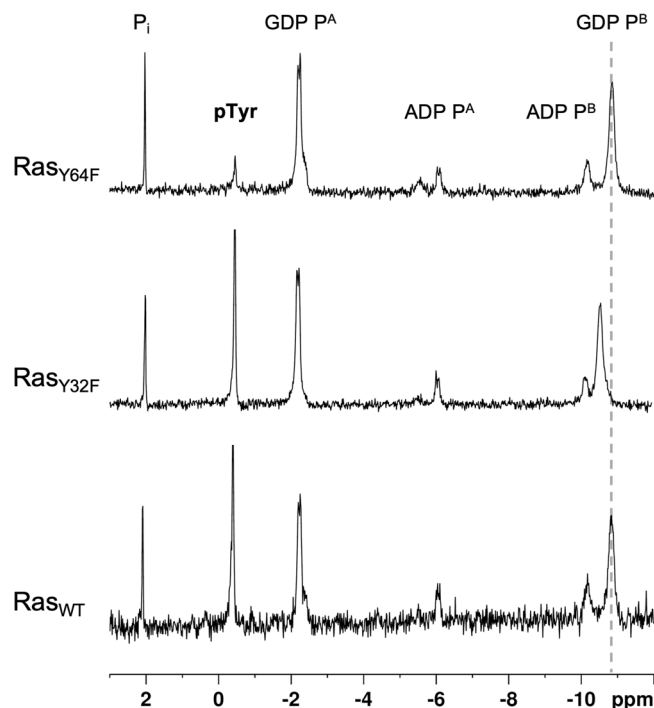


**Fig. 1**  $^{31}\text{P}$  NMR spectra of Src-mediated Ras phosphorylation. Ras<sub>WT</sub>, Ras<sub>Y32F</sub> or Ras<sub>Y64F</sub> (1.0 mM) were incubated with Src (20  $\mu\text{M}$ ) and phosphorylation buffer (ATP 5 mM, Tris-HCl 25 mM, pH = 7.6, NaCl 200 mM, MgCl<sub>2</sub> 5 mM) at 4 °C for 16 h. ATP, ADP and inorganic phosphate were largely removed by buffer exchange to avoid signal overlap for clarity.

**A GDP-BeF<sub>3</sub><sup>-</sup> complex delivers conformational changes different from non-hydrolysable GTP analogues.** After unsuccessful attempts of crystallising a BeF<sub>3</sub><sup>-</sup> GSA complex by co-crystallising Ras<sub>WT</sub>-GDP with Be<sup>2+</sup> and F<sup>-</sup>, we adopted a new approach by soaking Ras<sub>WT</sub>-GDP apo crystals with 50 mM BeCl<sub>2</sub> and 0.8 M NH<sub>4</sub>F for 1 to 2 min followed by flash freezing. We successfully obtained a BeF<sub>3</sub><sup>-</sup> structure for Ras<sub>WT</sub>-GDP-BeF<sub>3</sub><sup>-</sup> GSA complex (1.35 Å resolution, PDB: 8CNJ, Table 1, Supplementary Data 1). In this complex, the  $\alpha$ 2-helix (residues 66–74), which overlaps with Switch II in sequence, deviates from the one in the Ras-GDP structure by 42° but it adopts a conformation highly similar to the GTP- or GTP analogue-bound unphosphorylated Ras structures with an angle difference of <7° (Fig. 2a, Supplementary Figure 4, Table 2). This demonstrates this Ras<sub>WT</sub>-GDP-BeF<sub>3</sub><sup>-</sup> complex is mimicking a GTP-bound GSA state. This is also echoed by the high B-factor of Switch II observed, showing more mobility around the Switch II region than the rest of the protein (Fig. 3b), similar to the observation in the structure for the RhoA/RhoGAP product complex with both the GDP and P<sub>i</sub> bound, where the inorganic phosphate was also introduced by ligand soaking<sup>32</sup>. However, different from the GMPPCP (PDB: 121P) or GMPPNP-bound (PDB: 5P21) structures of Ras<sub>WT</sub>, our BeF<sub>3</sub><sup>-</sup> structure has well-defined electron densities for both Switch I and Switch II, in which Y32 donates an H-bond to F<sup>3</sup> and also accepts an H-bond from Q61 to the phenolic-OH of Y32. Thus, both Y32 and Q61 adopt a “closed” conformation (Fig. 2b). This is significantly different from the Y32 and Q61 conformations in other GSA structures of Ras with non-hydrolysable GTP analogues or by cryo techniques from a caged GTP analogue<sup>33</sup> (Fig. 3a). In the Ras-GMPPCP (PDB: 121P) and Ras-GMPPNP (PDB: 5P21, 4RSG) GSA complexes, the Y32 and Q61 are in a completely “open” conformation.

**Table 1** X-ray data collection, processing, and refinement statistics.

PDB	HRas <sub>Y64F</sub> -GDP apo 8BWG	HRas <sub>WT</sub> -GDP-BeF <sub>3</sub> <sup>-</sup> 8CNJ	HRas <sub>Y64F</sub> -GDP-BeF <sub>3</sub> <sup>-</sup> 8CNN
<b>Crystal Data</b>			
Wavelength	0.976 Å	0.976 Å	0.976 Å
Space group	H 3 2	P 21 21 21	H 3 2
<i>a</i> , <i>b</i> , <i>c</i> (Å)	92.66, 92.66, 119.32	45.43, 51.96, 136.15	87.77 87.77 132.38
$\alpha$ , $\beta$ , $\gamma$ (°)	90.00, 90.00, 120.00	90.00, 90.00, 90.00	90.00, 90.00, 120.00
Resolution (Å)	47.92–1.32	48.59–1.35	49.92–1.48
<i>R</i> <sub>merge</sub>	0.041	0.056	0.033
<i>I</i> / sig( <i>I</i> )	28.6 (1.1)	13.7 (1.4)	15.8 (1.2)
CC(1/2)	1.000 (0.577)	0.999 (0.598)	1.000 (0.559)
Completeness (%)	99.2 (91.0)	96.2 (68.4)	100.0 (100.0)
<b>Refinement</b>			
Unique reflections	45988 (2073)	69077 (2387)	32936 (1622)
<i>R</i> <sub>work</sub> / <i>R</i> <sub>free</sub>	0.135 / 0.174	0.144 / 0.183	0.138 / 0.176
<b>No. atoms</b>			
Protein	1335	2707	2669
Ligand/ion	33 / 1	64 / 2	140 / 1
Water	131	260	123
<b>B-factors</b>			
Protein	25.65	20.99	24.07
Ligand/ion	24.28 / 20.97	14.16 / 14.95	39.8 / 16.43
Water	37.45	34.49	36.09
<b>RMS deviations</b>			
Bond lengths (Å)	0.0097	0.0137	0.0118
Bond angles (°)	1.607	1.750	1.637

Values in parentheses are for the highest-resolution shell.

In the Ras-GTP $\gamma$ S GSA complex (PDB: 5VQ6), Y32 and Q61 are both disordered and incapable of providing any information.

Since the overall conformations of the GTP analogues are close to that of our BeF<sub>3</sub><sup>-</sup> complex structure, this closure of Y32 and Q61 must relate to the electron density of the surrogate  $\gamma$ -phosphoryl group atoms. Numerous computational studies based on these GTP analogue structures have concluded that the slow, intrinsic hydrolysis of GTP by Ras involves a solvent-assisted pathway via a “2 W” mechanism<sup>34,35</sup>, with partial support from a GTP-bound structure from a caged GTP analogue<sup>33</sup>. Calculations of conformational effects by PTMs and mutations of Ras have also been based on structures using non-hydrolysable GTP analogues<sup>36,37</sup>. Therefore, it is highly significant that in our Ras<sub>WT</sub>-GDP-BeF<sub>3</sub><sup>-</sup> GSA complex structure there is no second water molecule within 7.8 Å of P<sup>G</sup>. Only the isolated nucleophilic water is in a near-attack conformation (NAC) at P<sup>G</sup> along with the two waters closely coordinated to the octahedral catalytic Mg<sup>2+</sup>. This NAC water has an in-line angle (O<sup>3B</sup>-Be-Ow) 161° and is 3.5 Å from the beryllium atom. It donates an H-bond directly to T35 and F<sup>3</sup> and accepts a H-bond from Q61 (Fig. 2b). This highlights the different conformational details provided by GDP-BeF<sub>3</sub><sup>-</sup> and GTP analogues might lead to different mechanistic conclusions when alternative H-bonding patterns from residues G60 and Q61 are included in the QM zone<sup>15,38–40</sup>.

**$^{19}\text{F}$  NMR of BeF<sub>3</sub><sup>-</sup> GSA complexes capture both “open” and “closed” conformations.** Compared to crystal structures providing a snapshot of a conformation, solution  $^{19}\text{F}$  NMR has the unique advantage of detecting subtle conformational changes via chemical shift changes<sup>17,41</sup>. It can also capture minor conformations in phosphoryl transfer proteins that switch between several conformations because of its high sensitivity<sup>25,27</sup>.

Furthermore, by comparing the  $^{19}\text{F}$  chemical shifts of the same resonance measured in 10%  $\text{D}_2\text{O}$  and 90–100%  $\text{D}_2\text{O}$ , solvent-induced isotope shift (SIIS) can be calculated which accurately reflects the number and orientation of H-bond donors around each fluorine<sup>42</sup>. To assess whether the structural changes reflected by the  $\text{BeF}_3^-$  GSA structure are genuinely caused by Y64 phosphorylation and not by crystallographic artefacts, we investigated this  $\text{BeF}_3^-$  complex in solution  $^{19}\text{F}$  NMR with presaturation on free fluoride resonance at  $-120$  ppm. The pre-saturated  $^{19}\text{F}$  NMR spectrum of the  $\text{Ras}_{\text{WT}}\text{-GDP-BeF}_3^-$  complex shows three major well-resolved peaks for the protein-bound  $\text{BeF}_3^-$  moiety (Fig. 4a), outside the known range ( $-163$  to  $-170$  ppm) for free  $\text{BeF}_x$  species. The signal of  $\text{F}^1$  at  $-176.3$  ppm is significantly more upfield than the other resonances and has 0.3 ppm SIIS, indicating that it has a relatively high electron density and low proton density. It is thus assigned to  $\text{F}^1$ , coordinated to the catalytic magnesium<sup>25,26,28</sup>.  $\text{F}^2$  at  $-152.3$  ppm and  $\text{F}^3$  at  $-160.4$  ppm are also assigned by a combination of SIIS and a partial deuteration strategy (Table 3, Supplementary Figure 5)<sup>19,28</sup>. In particular, the

$^{19}\text{F}$  resonance of  $\text{F}^2$ , H-bonded to the K16 ammonium group, is differentially shifted by rotationally averaged HHH, HHD, HDD, and DDD congeners, leading to an unresolved peak in 10%, 50% and 95%  $\text{D}_2\text{O}$  buffers. By contrast,  $\text{F}^3$ , coordinated by two well-defined H-bonds from Y32 and the nucleophilic water, shows a resolved resonance at 50%  $\text{D}_2\text{O}$ <sup>19,28</sup>.

The  $\text{Ras}_{\text{WT}}\text{-GDP-BeF}_3^-$  GSA complex exhibited a minor set of  $^{19}\text{F}$  signals comprising  $\sim 10\%$  of the population, characterised by three resonances at  $-155.3$  ppm,  $-162.6$  ppm, and  $-183.0$  ppm. Notably, all three resonances are shifted 3–7 ppm upfield relative to those of the major species (Fig. 4a), implying increased shielding for all three fluorines of  $\text{BeF}_3^-$  in this minor species, a sign of the reduced extent of H-bonding to the  $\text{BeF}_3^-$  moiety. To investigate whether this minor species originates from the “open” conformation that has been crystallised in the structure of  $\text{Ras}_{\text{Y32F}}\text{-GMPPNP}$  (PDB: 3K9N), where the benzyl side chain adopts an “open” conformation, we introduced a Y32F mutation and generated the  $\text{Ras}_{\text{Y32F}}\text{-GDP-BeF}_3^-$  GSA complex, monitored using  $^{19}\text{F}$  NMR (Fig. 4b). Applying presaturation on the unbound fluoride resonance at  $-120$  ppm was essential to distinguish the fluorine resonances associated with Ras from the free  $\text{BeF}_x$  resonances present in the solution around  $-167$  ppm (Supplementary Figure 6). The  $^{19}\text{F}$  NMR spectrum of the  $\text{Ras}_{\text{Y32F}}\text{-GDP-BeF}_3^-$  GSA complex reveals a distinct overall profile: The trio of resonances, aligned with chemical shifts akin to the minor species in the  $\text{Ras}_{\text{WT}}\text{-GDP-BeF}_3^-$  GSA complex, emerged as predominant by integrations. In contrast, fluorine  $\text{F}^3$  from the second set of peaks, exhibiting chemical shifts more similar to the resonances of the “closed” conformation, has shifted downfield by 7.5 ppm and fused with  $\text{F}^2$  (Table 3). This is likely due to a water molecule assuming the role of an H-bond donor to  $\text{F}^3$ , analogous to the phenolic  $-\text{OH}$  of Y32. This strongly underscores the pivotal role of Y32  $-\text{OH}$  in neutralising the negative charge on the  $\gamma$ -phosphate during intrinsic GTP hydrolysis. It is noteworthy that, at equal component concentrations, the significantly lower signal-to-noise ratio in the  $\text{Ras}_{\text{Y32F}}\text{-GDP-BeF}_3^-$  GSA implies that the occupancy of  $\text{BeF}_3^-$  is less than 100%, unlike the  $\text{Ras}_{\text{WT}}\text{-GDP-BeF}_3^-$  complex, suggesting that Y32  $-\text{OH}$  also contributes to the binding of both  $\text{BeF}_3^-$  and GTP. The 10% population of  $\text{Ras}_{\text{WT}}\text{-GDP-BeF}_3^-$  GSA in “open” conformation explains why we could not crystallise this complex by co-crystallisation after many attempts and why its structure has been missing in the PDB.

**$^{19}\text{F}$  NMR of metal fluoride complexes identify a structurally invisible effect of phosphorylation of Ras Y64.** We next examined the impact of Y64 phosphorylation by investigating the  $\text{Ras}_{\text{PY64}}\text{-GDP-BeF}_3^-$  GSA complex via solution  $^{19}\text{F}$  NMR. The  $^{19}\text{F}$  NMR spectrum shows three major well-resolved resonances. Notably, they show small upfield shifts of 0.6 and 0.5 ppm for  $\text{F}^1$  and  $\text{F}^2$ , respectively, compared to the  $\text{Ras}_{\text{WT}}\text{-GDP-BeF}_3^-$  complex. Conversely,  $\text{F}^3$  experiences a 0.5 ppm downfield shift (Table 3, Fig. 4c). Although these chemical shift changes are marginal, they

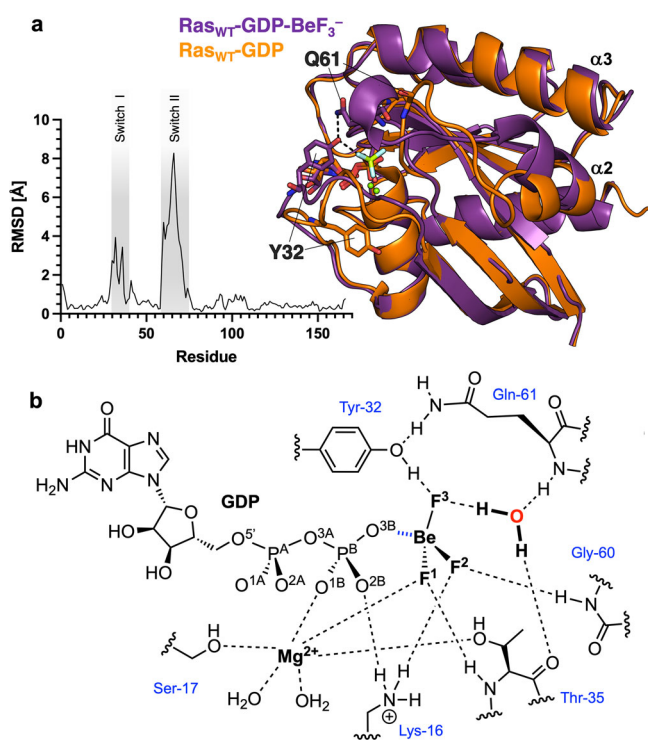


**Fig. 2**  $\text{Ras}_{\text{WT}}\text{-GDP-BeF}_3^-$  GSA complex. **a** Overlay of  $\text{Ras}_{\text{WT}}\text{-GDP}$  (orange, PDB: 4Q21) and  $\text{Ras}_{\text{WT}}\text{-GDP-BeF}_3^-$  (purple, PDB: 8CNJ). RMSD for the structure alignment is plotted for each residue. The major conformational changes are induced in the Switch I and Switch II regions. **b** H-bond interactions for the  $\text{Ras-GDP-BeF}_3^-$  GSA complex were observed in its structure.

**Table 2** Angle differences in  $\alpha 2$ -helix of the Switch II region for Ras structures.

	$\text{Ras}_{\text{PY64}}\text{-GDP-BeF}_3^-$	$\text{Ras}_{\text{WT}}\text{-GDP-BeF}_3^-$	$\text{Ras}_{\text{WT}}\text{-GTP}$	$\text{Ras}_{\text{WT}}\text{-GMPPNP}$	$\text{Ras}_{\text{WT}}\text{-GMPPCP}$	$\text{Ras}_{\text{PY64}}\text{-GDP}$
$\text{Ras}_{\text{WT}}\text{-GDP}$	34.57°	41.99°	37.13°	43.73°	42.09°	2.67°
$\text{Ras}_{\text{PY64}}\text{-GDP}$	32.41°	40.44°	35.35°	41.99°	43.80°	
$\text{Ras}_{\text{WT}}\text{-GMPPCP}$	12.89°	3.29°	6.82°	0.65°		
$\text{Ras}_{\text{WT}}\text{-GMPPNP}$	12.43°	3.80°	6.65°			
$\text{Ras}_{\text{WT}}\text{-GTP}$	7.55°	6.27°				
$\text{Ras}_{\text{WT}}\text{-GDP-BeF}_3^-$	13.53°					

$\text{Ras}_{\text{PY64}}\text{-GDP-BeF}_3^-$ , PDB: 8C9N;  $\text{Ras}_{\text{WT}}\text{-GDP-BeF}_3^-$ , PDB: 8CNJ;  $\text{Ras}_{\text{WT}}\text{-GTP}$ , PDB: 1QRA (caged-GTP analogue);  $\text{Ras}_{\text{WT}}\text{-GMPPNP}$ , PDB: 121P;  $\text{Ras}_{\text{WT}}\text{-GMPPCP}$ , PDB: 5P21;  $\text{Ras}_{\text{PY64}}\text{-GDP}$ , PDB: 8B0S;  $\text{Ras}_{\text{WT}}\text{-GDP}$ , PDB: 4Q21. Data are colours coded by the level of difference for clarity.

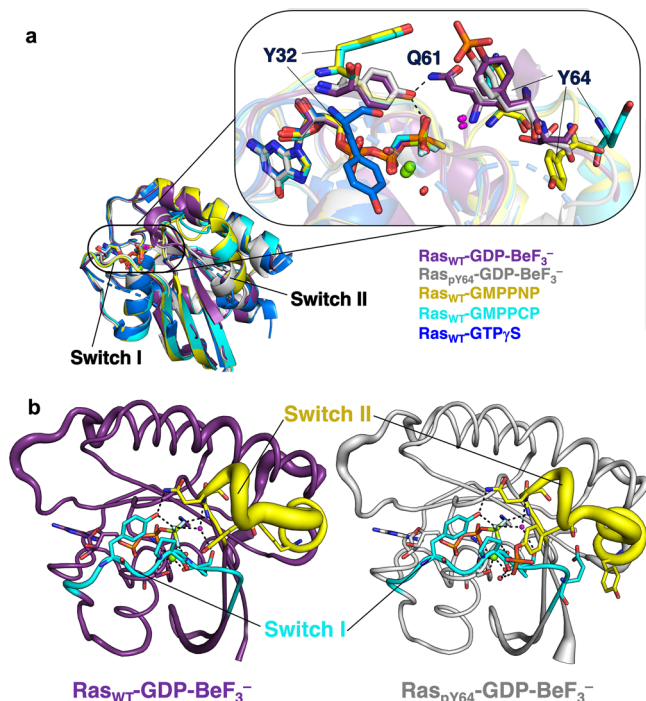


**Fig. 3 Comparison of GDP-BeF<sub>3</sub><sup>-</sup> GSA complex structures of Ras to other Ras GSA structures with non-hydrolysable GTP analogues or caged GTP analogues.** **a** Overlay of different Ras structures (Ras<sub>WT</sub>-GDP-BeF<sub>3</sub><sup>-</sup> PDB: 8CNJ, Ras<sub>pY64</sub>-GDP-BeF<sub>3</sub><sup>-</sup> PDB: 8CNN, Ras<sub>WT</sub>-GTP PDB: 1QRA, Ras<sub>WT</sub>-GMPPCP PDB: 121P, Ras<sub>WT</sub>-GMPPNP PDB: 5P21, Ras<sub>WT</sub>-GTPγS PDB: 5VQ6) show direct coordination of Y32 for the Ras-BeF<sub>3</sub><sup>-</sup> GSA structures and a more “open” Y32 conformation for the Ras structures complexed with non-hydrolysable GTP analogues. **b** B-factor putty models of Ras<sub>WT</sub>-GDP-BeF<sub>3</sub><sup>-</sup> (purple) and Ras<sub>pY64</sub>-GDP-BeF<sub>3</sub><sup>-</sup> (grey) show increased mobility for the Switch II region.

show only a small impact of Y64 phosphorylation on the catalytic site with no direct interaction existing between the BeF<sub>3</sub><sup>-</sup> moiety and the negatively charged phosphate on the phenolic -OH group of Y64. The average upfield shift of 0.2 ppm across the three resonances, compared to Ras<sub>WT</sub>-GDP-BeF<sub>3</sub><sup>-</sup>, likely signifies a marginal increase in electron density on the three oxygen atoms within the γ-phosphate. This effect might induce a slightly increased repulsion during nucleophilic attack, thus rationalising the observed 3-fold reduction in intrinsic GTPase activity following phosphorylation. Moreover, the three resonances from the Ras<sub>pY64</sub>-GDP-BeF<sub>3</sub><sup>-</sup> complex have an average 0.70 ppm half-height line width, larger than the mean 0.48 ppm of the Ras<sub>WT</sub>-GDP-BeF<sub>3</sub><sup>-</sup> complex. This indicates a slightly slower exchange rate of the BeF<sub>3</sub><sup>-</sup> moiety with free fluoride and free BeF<sub>x</sub> species in the Ras<sub>pY64</sub>-GDP-BeF<sub>3</sub><sup>-</sup> complex on the NMR time scale. Furthermore, a noteworthy but subtle observation emerges: the ratio between major and minor forms, calculated from the averaged integrations of F<sup>1</sup> and F<sup>2</sup>, decreases by ~10%. This signals an increased ‘open’ conformation population in Ras<sub>pY64</sub>-GDP-BeF<sub>3</sub><sup>-</sup> following Y64 phosphorylation. Considering the pM affinity binding of GDP to Ras, the accelerated exchange rate of BeF<sub>3</sub><sup>-</sup> and increased population of open conformation further strengthens the assertion of a 2.6-fold increase in intrinsic nucleotide exchange rate upon phosphorylation (primarily on Y64), as also corroborated by NMR measurements<sup>7</sup>.

To investigate the impact of Y64 phosphorylation on GAP binding, we also attempted to form an MF<sub>x</sub> TSA complex with Ras<sub>pY64</sub> and RasGAP monitored by <sup>19</sup>F NMR (Supplementary Figure 7). However, our attempts were unsuccessful, which stands

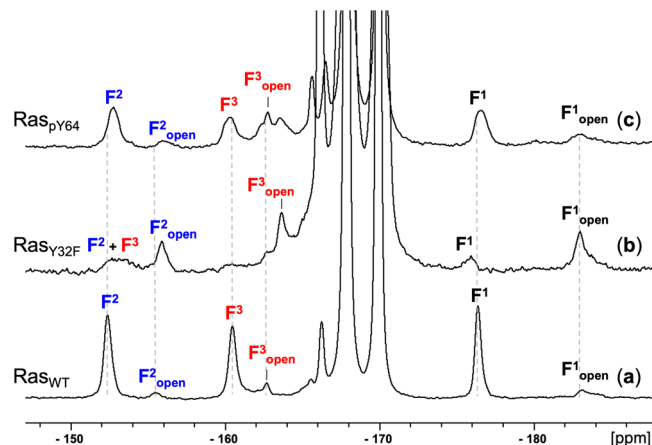


**Fig. 4 <sup>19</sup>F NMR spectra of GDP-BeF<sub>3</sub><sup>-</sup> GSA complexes.** **a** Ras<sub>WT</sub>-GDP-BeF<sub>3</sub><sup>-</sup> complex, **b** Ras<sub>Y32F</sub>-GDP-BeF<sub>3</sub><sup>-</sup> complex, and **c** HRas<sub>pY64</sub>-GDP-BeF<sub>3</sub><sup>-</sup> complex. All spectra were acquired with presaturation on the unbound fluoride resonance at -120 ppm. Samples consisted of 0.8–1.0 mM Ras protein in buffers of 25 mM Tris-HCl pH = 7.0 with 10% D<sub>2</sub>O with 3 mM BeCl<sub>2</sub>, 30 mM NH<sub>4</sub>F, and 5 mM MgCl<sub>2</sub>.

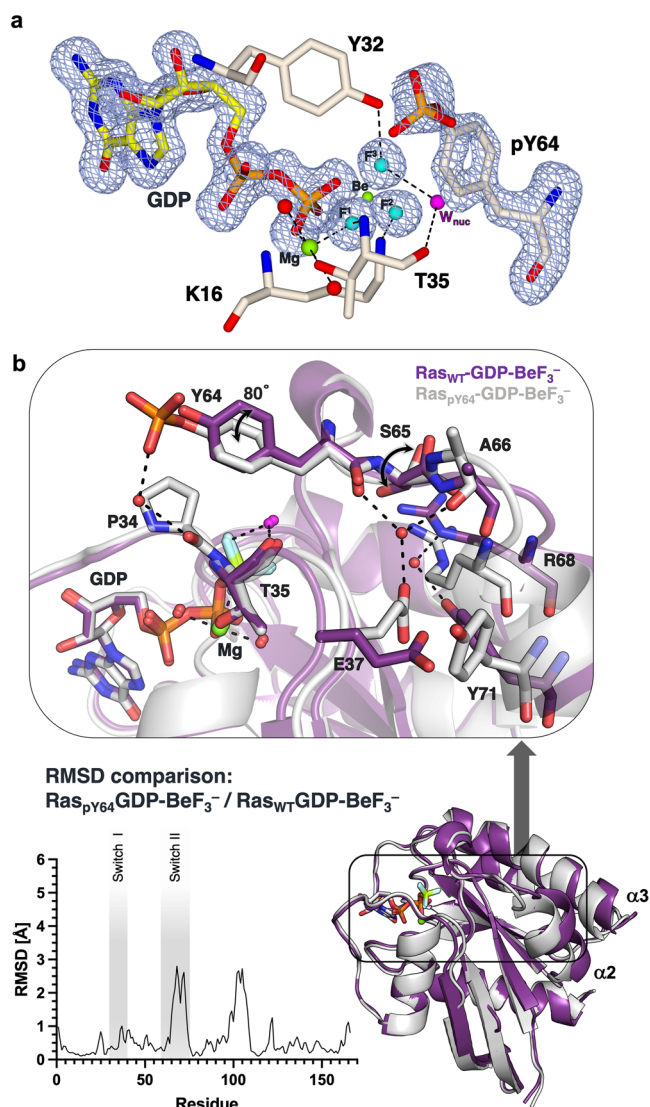
in stark contrast to the easily formed RasGAP/Ras-GDP-“AlF<sub>3</sub><sup>0</sup>” TSA complex (PDB: 1WQ1) observed by both crystallography<sup>43</sup> and backed up by our <sup>19</sup>F NMR test (Supplementary Figure 8). This confirms phosphorylation on Y64 could disrupt productive interactions with RasGAP, likely due to the steric hindrance because Y64 forms a H-bond with L902 of RasGAP in the RasGAP/Ras-GDP-AlF<sub>3</sub><sup>0</sup> complex structure.

**Effect of phosphorylation of tyrosine64 revealed by the structure of Ras<sub>pY64</sub>-GDP-BeF<sub>3</sub><sup>-</sup> GSA complex.** To gain atomistic insight into how phosphorylation of Y64 could influence intrinsic GTP hydrolysis and nucleotide exchange rates with phosphorylated Ras, we initially assessed the stability of phosphorylated Ras. Our results indicated that monophosphorylated Ras remained stable in buffer for over a week, rendering it suitable for subsequent crystallisation trials (Supplementary Figure 9). We first crystallised the apo Ras<sub>pY64</sub>-GDP apo structure with commercial crystallisation screens. This structure was solved at 1.32 Å resolution (Table 1, PDB: 8BWG, Supplementary Data 2) but residues 60–64 as a key part of the Switch II loop do not have clear electron density. Thus, it cannot provide the accurate location and coordination of pY64. α2-Helix adopts a conformation that is highly similar to other GDP-bound product structures of Ras with an angle difference of <5° degree (Table 2).

We then obtained a BeF<sub>3</sub><sup>-</sup> GSA complex by soaking Ras<sub>pY64</sub>-GDP apo crystals with 50 mM BeCl<sub>2</sub> and 0.8 M NH<sub>4</sub>F for 1 to 2 min before flash-freezing. The Ras<sub>pY64</sub>-GDP-BeF<sub>3</sub><sup>-</sup> GSA complex structure formed diffracts to 1.48 Å resolution (Table 1, PDB: 8CNN, Supplementary Data 3). While different from the Ras<sub>pY64</sub>-GDP apo structure, the Ras<sub>pY64</sub>-GDP-BeF<sub>3</sub><sup>-</sup> complex has well-defined electron densities for the flexible Switch II loop including the whole pY64, and the ordered Switch I loop in a “closed-up” conformation, where Y32 directly donates an H-bond to F<sup>3</sup> (Fig. 5a, Supplementary Figure 10). Compared to the unphosphorylated Ras<sub>WT</sub>-GDP-BeF<sub>3</sub><sup>-</sup> GSA complex (backbone atom RMSD 0.766 Å, Supplementary Figure 11), our Ras<sub>pY64</sub>-GDP-BeF<sub>3</sub><sup>-</sup> GSA structure exhibits noticeable conformational changes (Fig. 5b). Originating from the phosphate in pY64, these extensive conformational shifts (spanning up to 28 Å) are a result of the alteration (80°) in the rotameric angle of the phenolic ring. This change is facilitated by an interaction with the backbone carbonyl

**Table 3**  $^{19}\text{F}$  NMR chemical shift ( $\delta$ ) comparison of GDP-BeF $_3^-$  GSA complexes and their respective linewidths in 10% D $_2$ O.

	Ras $_{\text{WT}}$ -GDP-BeF $_3^-$		Ras $_{\text{Y32F}}$ -GDP-BeF $_3^-$		Ras $_{\text{pY64}}$ -GDP-BeF $_3^-$	
	$\delta$ [ppm]	linewidth [ppm] <sup>a</sup>	$\delta$ [ppm]	linewidth [ppm] <sup>a</sup>	$\delta$ [ppm]	linewidth [ppm] <sup>a</sup>
F1	-176.3	0.45	-175.9	0.89	-176.9	0.57
F2	-152.5	0.50	-152.9	1.92	-152.0	0.82
F3	-160.5	0.51			-161.0	0.71

<sup>a</sup>Full width at half peak height.**Fig. 5** The structure of the Ras $_{\text{pY64}}$ -GDP-BeF $_3^-$  GSA complex. **a** Active site of Ras $_{\text{pY64}}$ -GDP-BeF $_3^-$ .  $F_0$ - $F_c$  omit map for GDP, BeF $_3^-$  and pY64 are contoured at  $3\sigma$ ,  $0.330 \text{ \AA}^{-3}$  (light blue mesh). Key neighbouring residues are shown in sticks. H-bonds coordinating to BeF $_3^-$  are shown as dashed lines. **b** Overlay of Ras $_{\text{WT}}$ -GDP-BeF $_3^-$  (purple) and Ras $_{\text{pY64}}$ -GDP-BeF $_3^-$  (grey). RMSD for the structure alignment is plotted for each residue.

group of Switch I P34, mediated through a water molecule. In turn, this changes the dihedral angle  $\psi$  (O-C-C $_{\alpha}$ -N) of S65 from  $39.3^\circ$  to  $173.5^\circ$ , and the deviation of the  $\alpha 2$ -helix is further propagated throughout from the N-end of the  $\alpha 2$ -helix (residues 64–74) to the C-end of the  $\alpha 3$ -helix (residues 87–104) by a shift of by  $2.5 \text{ \AA}$  (Fig. 5b). Indeed, T74 and M67 have shown noticeable chemical shift changes in  $^1\text{H}$ - $^{15}\text{N}$  HSQC in solution after

phosphorylation<sup>7</sup>. The distinctive water-mediated interaction between the negatively charged phosphate on pY64 in Switch II and P34 in Switch I suggests its potential to obstruct the entry of a second water molecule into the active site. This observation offers another plausible rationale for the observed three-fold reduction in intrinsic hydrolysis rate<sup>7</sup>.

The diminished interaction between phosphorylated Ras and Raf-RBD has been explored by molecular dynamics, suggesting that the heightened flexibility of phosphorylated Y32 hinders Raf binding<sup>7</sup>. When Ras $_{\text{pY64}}$ -GDP-BeF $_3^-$  is aligned with Ras-GMPPNP-Raf complex structure (PDB: 4G0N), a noticeable alteration becomes evident. The backbone carbonyl group of pY64 reorients itself by forming a hydrogen bond with a water molecule, which simultaneously participates in H-bonding with the carbonyl group of A66 and the carboxylate sidechain of E37. The key interactions involving E37 of Ras and R59 and R67 of Raf are disrupted due to the substantial changes in the orientations of both E37 and Y71 following Y64 phosphorylation (Fig. 6). Our structure offers an additional explanation for the significant reduction in affinity between the downstream effector Raf and phosphorylated Ras, mediated by Src. This reduction is attributed to the extensive long-range conformational alterations resulting from the Y64 phosphorylation<sup>7</sup>.

## Conclusion

In this study, we have substantiated Y64 as the predominant site of phosphorylation by Src. This finding suggests that Ras likely exerts its biological function primarily in its mono-phosphorylated form. Making new use of pM GDP binding and readily available Be $^{2+}$  and F $^-$  salts, we successfully obtained a GDP-BeF $_3^-$  GSA complex for both unphosphorylated and Y64-phosphorylated Ras. The large conformational alterations induced by BeF $_3^-$  within the crystalline structure are of substantial significance. This demonstrates new efficacy and validity of a soaking approach in generating GDP-BeF $_3^-$  GSA complexes for small G proteins from their GDP-bound structures. It offers a convenient strategy for structural biological inquiries, without the need to carry out nucleotide exchange with non-hydrolysable GTP analogues. Our investigation reveals that the impact of Src-mediated Y64 phosphorylation on Ras extends beyond the Switch I and II regions. It encompasses broader steric and conformational effects, significant for the biological roles of this crucial PTM of Ras, especially for its interactions with effector proteins such as Raf. These two BeF $_3^-$  GSA complexes both capture a “closed” conformation where Y32 in Switch I directly interacts with Q61 in Switch II by H-bonding, different from other ground state conformations as depicted by caged-GTP, GMPPNP, GMPPCP, or GTP $\gamma$ S. Furthermore, the utility of  $^{19}\text{F}$  NMR is extended to elucidate the underlying molecular basis of conformational changes induced by PTMs, which might not be captured by high-resolution structures. It serves as a precedent for its application to the investigation of other PTMs, such as S-nitrosylation on C118<sup>44</sup>. Indeed, utilising  $^{19}\text{F}$  NMR on BeF $_3^-$  GSA complexes reveals that Switch I predominantly adopts a

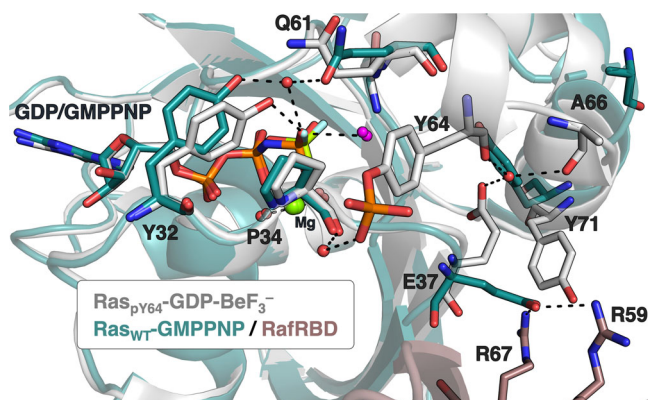


**Fig. 6 Insights of the impact of Y64 phosphorylation on Raf binding.** Comparison of structures for Ras<sub>Y64</sub>-GDP-BeF<sub>3</sub><sup>-</sup> (PDB: 8CNN, grey) and Ras<sub>WT</sub>-GMPPNP/RafRBD (PDB: 4GON, green/brown). Nucleophilic water is shown in magenta.

“closed” conformation (~90% occupancy) in solution. Our study underscores the utility of BeF<sub>3</sub><sup>-</sup> complexes to reveal distinct conformational nuances opaque with non-hydrolysable GTP analogues. Finally, BeF<sub>3</sub><sup>-</sup> GSA structures fill a crucial gap for molecular docking in Ras-targeted drug discovery and present valuable starting points for computational investigations, quantum mechanics/molecular mechanics (QM/MM) and molecular dynamics (MD), which can deliver disparate mechanistic and conformational insights.

## Methods

**Molecular cloning.** pGEX-RasGAP334<sub>(714–1047)</sub> encoding the human RasGAP domain (Uniprot: P20936) from residues 714 to 1047 and ptac-HRas<sub>(1–166)</sub> encoding the human HRas (Uniprot: P01112) from residues 1 to 166 were kindly provided by the Wittinghofer lab<sup>43</sup>. ptac-HRas<sub>(1–166)</sub>-Y32F and ptac-HRas<sub>(1–166)</sub>-Y64F were generated by site-directed mutagenesis from ptac-HRas<sub>(1–166)</sub> using PrimestarMax (Takara Bio Inc.) and sequenced to confirm the desired mutation. Plasmids pET28-cSrc<sub>(251–533)</sub> encoding the gene of chicken Src kinase (Uniprot: P00523) catalytic domain (only three amino acids differ from its human homologue) and pCDFDUET-YoPH encoding a tyrosine phosphatase YoPH were a generous gift from Dr Feng Ni (Ningbo University, China)<sup>45</sup>.

**Gene expression and protein purification.** HRas(1–166): *E. coli* BL21(DE3) cells were transformed with ptac-HRas<sub>(1–166)</sub> plasmid, plated onto LB agar plates (100 µg/mL ampicillin) and grown overnight at 37 °C. A single colony was used to inoculate 30 mL of LB media (100 µg/mL ampicillin) and incubated at 37 °C overnight. This culture was used to inoculate LB medium (100 µg/mL ampicillin) at a 1:100 ratio. The culture was grown at 37 °C to an OD<sub>600</sub> between 0.6 and 0.8 and gene expression was induced with 1.0 mM IPTG. The culture was shaken at 25 °C for 18 h and cells were harvested by centrifugation (7000 g, 4 °C, 20 min). The cell pellet was either stored at -80 °C or processed directly after centrifugation. The cell pellet was resuspended in buffer A (Tris-HCl 25 mM, pH = 7.6, MgCl<sub>2</sub> 5 mM, DTT 1 mM) and supplemented with 1 mM PMSF. The cells were lysed by sonication (4 min sonication time, 2 s on and 8 s off) and cell debris removed by centrifugation (32000 g, 4 °C, 40 min). The supernatant was filtered and loaded on a DEAE column, washed with 3 CV lysis buffer and eluted by applying a gradient of 0–100% elution buffer (Tris-HCl 25 mM, pH = 7.6, NaCl 200 mM, MgCl<sub>2</sub> 5 mM, DTT 1 mM) over 8 CV. The eluted protein fractions were

pooled and concentrated. Finally, the target protein was purified on a SEC75 26/60 column and stored at -80 °C. The same procedure was used for ptac-HRas<sub>(1–166)</sub>-Y32F and ptac-HRas<sub>(1–166)</sub>-Y64F.

RasGAP<sub>334</sub>(714–1047): *E. coli* BL21(DE3) cells were transformed with pGEX-2T-RasGAP<sub>(714–1047)</sub> plated onto LB agar plates (100 µg/mL ampicillin) and grown overnight at 37 °C. A single colony was used to inoculate 30 mL of LB media (100 µg/mL ampicillin) and the culture was shaken at 37 °C overnight. This culture was used to inoculate LB media (ampicillin 100 µg/mL) at a 1:100 ratio. The culture was grown at 37 °C to an OD<sub>600</sub> between 0.6 and 0.8 and expression was induced with 1.0 mM IPTG. The culture was incubated at 18 °C for 18 h and cells were harvested by centrifugation (7000 g, 4 °C, 20 min). The cell pellet was resuspended in buffer A (Tris-HCl 50 mM, pH = 7.6, NaCl 150 mM, MgCl<sub>2</sub> 5 mM, DTT 1 mM) and supplemented with 1 mM PMSF. Cells were lysed by sonication (4 min sonication time, 2 s on and 8 s off) and cell debris was removed by centrifugation (32000 g, 4 °C, 40 min). The supernatant was filtered and loaded on GST resin (GST-HP resin, Cytiva, United States). The resin was incubated on a tube roller at 4 °C for 60 min and washed with 5 CV buffer A. The target protein was eluted over 3 CV with buffer B (Tris-HCl 50 mM, pH = 7.6, NaCl 150 mM, MgCl<sub>2</sub> 5 mM, DTT 1 mM, glutathione 10 mM) and buffer exchanged into buffer A. To cleave the GST-tag the protein solution was incubated at 4 °C with 25 NIH units of thrombin (T7326-1KU, Sigma Aldrich, United States). Progress of the cleavage reaction was controlled via SDS-PAGE and further thrombin was added as required. Upon completion of the cleavage reaction, the protein solution was incubated with GST resin at 4 °C. After 60 min the flow-through was collected and concentrated. Finally, the target protein was purified on a SEC75 26/60 column and stored at -80 °C.

Src(251–533): The catalytic domain of chicken Src was prepared following the protocol described in the literature<sup>45</sup>. *E. coli* BL21(DE3) cells were co-transformed with pET28-cSrc<sub>(251–533)</sub> and pCDFDuet-YoPH and incubated on LB agar (50 µg/mL kanamycin and 50 µg/mL streptomycin) overnight at 37 °C. A single colony was used to inoculate 30 mL of LB media (50 µg/mL kanamycin and 50 µg/mL streptomycin) and the culture was shaken at 180 rpm at 37 °C overnight. This culture was used to inoculate TB medium (50 µg/mL kanamycin and 50 µg/mL streptomycin) at a 1:100 ratio. The culture was grown at 37 °C to an OD<sub>600</sub> between 1.0 and 1.2 and gene expression was induced with 0.2 mM IPTG. The culture was incubated at 18 °C for 16 h and cells were harvested by centrifugation (7000 g, 4 °C, 20 min). The cell pellet was either processed directly after centrifugation or stored at -80 °C. The cell pellet was resuspended in buffer A (Tris-HCl 50 mM, pH = 8.0, NaCl 500 mM, imidazole 25 mM, glycerol 5% (v/v)) and supplemented with 1 mM PMSF. Cells were lysed by sonication (4 min sonication time, 2 s on and 8 s off) and cell debris removed by centrifugation (32000 g, 4 °C, 40 min). The supernatant was filtered and loaded on a Ni<sup>2+</sup>-NTA column (Cytiva, 5 mL FF HisTrap). After washing with 5 CV buffer A, the target protein was eluted by applying a gradient of 0–50% buffer B (Tris-HCl 50 mM, pH = 8.0, NaCl 500 mM, imidazole 500 mM, glycerol 5% v/v) over 30 CV. The eluted protein fractions were pooled, concentrated, and dialysed at 4 °C overnight against 20 volumes of buffer C (Tris-HCl 20 mM, pH = 8.0, 100 mM, DTT 1 mM, glycerol 5% v/v). The crude kinase was then loaded onto a Q column (Cytiva, HiTrap FF 5 mL) and eluted by applying a gradient of 0–40% buffer D (Tris-HCl 20 mM, pH = 8.0, NaCl 1.0 M, DTT 1 mM, glycerol 5% v/v). Fractions containing the kinase were pooled, further purified on a SEC75 16/60 column and stored at -80 °C.

**Ras phosphorylation assay by Src.** 500  $\mu\text{M}$  Ras-GDP was incubated for 2 h at 25 °C in assay buffer (Tris-HCl 25 mM pH = 7.6, NaCl 150 mM,  $\text{MgCl}_2$  5 mM, DTT 1 mM, ATP 4 mM, cSrc 20  $\mu\text{M}$ ). To remove excess ADP/ATP and quantify each Ras species, monophosphorylated Ras as the major species shown by the chromatogram was separated from unphosphorylated and double-phosphorylated species by ion-exchange chromatography on a 16  $\times$  100 mm Q FF 16/10 column. The chromatogram shows a major monophosphorylated peak, and two double-phosphorylated peaks as identified by MS. (Supplementary Figure 2, Supplementary Figure 12).

**Mass spectrometry (MS).** Ras<sub>WT</sub>, Ras variants and all the phosphorylated Ras species were subjected to MS for confirmation (Supplementary Figure 12). Liquid chromatography-mass spectrometry (LC-MS) was performed on a WATERS Synapt G2-Si quadrupole time-of-flight mass spectrometer coupled to a WATERS Acquity H-Class ultraperformance liquid chromatography (UPLC) system. The column was a WATERS Acquity UPLC protein BEH C4 (300 Å, 1.7  $\mu\text{m}$   $\times$  2.1 mm  $\times$  100 mm) operated in reverse phase and held at 60 °C. The gradient employed was 95% A to 35% A over 50 min, where A is water with 0.1%  $\text{HCO}_2\text{H}$  and B is acetonitrile with 0.1%  $\text{HCO}_2\text{H}$ . Spectra were collected in positive ionisation mode and analysed using WATERS MassLynx software version 4.1. Deconvolution of protein-charged states was obtained using the maximum entropy 1 processing software.

**Nuclear Magnetic Resonance (NMR) spectroscopy.** NMR spectra in this work have been recorded on a 500 MHz Bruker five-channel liquid-state spectrometer with a high sensitivity QXI cryoprobe. Chemical shifts ( $\delta$ ) are given in parts per million (ppm). All spectra were recorded at 20 °C. For the presaturation of the free fluoride signal, elective  $^{19}\text{F}$  irradiation was achieved with a continuous wave (power level of 42 dB) applied over the 1 s recycle delay at the frequency of free fluoride peak (-119.5 ppm). For samples with 90%  $\text{D}_2\text{O}$ , this frequency was adjusted to -121.5 ppm. Unless stated otherwise, all protein  $^{19}\text{F}$  NMR spectra were calibrated to an internal fluorobenzene standard at -113.79 ppm<sup>46</sup>.

**Stability of phosphorylation on Ras tyrosine.** The stability of phospho-Ras was determined by incubating 100  $\mu\text{M}$  monophosphorylated Ras-GDP in crystallisation buffer (HEPES-Na 20 mM, pH = 8.0,  $\text{MgCl}_2$  10 mM, NaF 20 mM). At regular intervals, 30  $\mu\text{L}$  aliquots were taken and mixed with SDS-PAGE loading buffer, heated to 95 °C for 3 min and stored at -80 °C until all time points could be analysed by SDS-PAGE (Supplementary Figure 9).

**Protein x-ray crystallography.** Protein crystallisation conditions were set up either using a Douglas Instruments ORYX4 or a SPTlabtech Mosquito Crystal system in either a hanging drop or sitting drop configuration. Microseeding was performed based on literature conditions<sup>47</sup>.

Ras<sub>pY64</sub>-GDP: Condition screening using a commercial crystal screen (Hampton Research, HR2-130) was initially for searching for a condition for the “Ras<sub>pY64</sub>-GDP-RasGAP<sub>334</sub>” complex but yielded a hit for Ras<sub>pY64</sub>-GDP under sitting drop conditions (drop size 600 nL) with a 1:1 ratio of protein solution (Ras<sub>pY64</sub>-GDP 400  $\mu\text{M}$ , RasGAP<sub>334</sub> 400  $\mu\text{M}$ , Na-HEPES 20 mM pH = 8.0,  $\text{MgCl}_2$  5 mM, NaF 20 mM) and precipitant (Na-citrate 100 mM pH = 5.6,  $\text{Li}_2\text{SO}_4$  1.0 M,  $\text{CaCl}_2$  200 mM). After three rounds of microseeding well-formed single crystals were obtained using 2.0  $\mu\text{L}$  sitting drops and a 1:1 ratio of protein stock (Ras<sub>pY64</sub>-GDP

400  $\mu\text{M}$ , RasGAP<sub>334</sub> 400  $\mu\text{M}$ , Na-HEPES 20 mM pH = 8.0, 5 mM  $\text{MgCl}_2$ , NaF 20 mM) and precipitant (Na-citrate 100 mM pH = 5.6,  $\text{Li}_2\text{SO}_4$  800 mM,  $\text{CaCl}_2$  200 mM). These were harvested using cryoprotectant (80% precipitant, 20% glycerol v/v) and used for data collection.

**Metal fluoride soaking.** Ras<sub>pY64</sub>-GDP- $\text{BeF}_3^-$  GSA complex: To obtain the Ras<sub>pY64</sub>-GDP apo crystals, protein stock (Ras<sub>pY64</sub> 400  $\mu\text{M}$ , Na-HEPES 20 mM pH = 8.0,  $\text{MgCl}_2$  5 mM, NaF 20 mM) was mixed with precipitant (100 mM NaOAc, pH = 4.5, 200 mM  $\text{Li}_2\text{SO}_4$ , 50% v/v PEG400) in a 1:1 ratio with a total drop size of 600 nL. Protein crystals were then soaked in the precipitant solution supplemented with 50 mM  $\text{BeCl}_2$  and 800 mM  $\text{NH}_4\text{F}$ .

Ras-GDP- $\text{BeF}_3^-$  GSA complex: Protein stock (Ras-GDP 400  $\mu\text{M}$ , Na-HEPES 20 mM pH = 8.0,  $\text{MgCl}_2$  5 mM, NaF 20 mM) was mixed with precipitant (30% v/v MPD, 100 mM imidazole, pH = 7.0) in a 1:1 ratio with a total drop size of 600 nL. Protein crystals were then soaked in the precipitant solution supplemented with 50 mM  $\text{BeCl}_2$  and 800 mM  $\text{NH}_4\text{F}$ .

The soaked crystals were subsequently flash-frozen using cryoprotectant (80% precipitant, 20% glycerol v/v) before data collection.

**Data collection, structure solution and refinement.** The datasets described in this report were collected at the Diamond Light Source, Didcot, Oxfordshire, U.K. on beamline I03. Data were integrated using XDS<sup>48</sup> and scaled/merged using AIMLESS<sup>49</sup> included in the CCP4 software suite xia2<sup>50</sup>. Data collection and refinement statistics are provided in Table 1. The structures were solved by molecular replacement using MOLREP<sup>51</sup> with one monomer of Ras in PDB: 1WQ1 as the model and refined with Refmac<sup>52</sup>.

Backbone RMSD for each pair of Ras structures were calculated by aligning the structures in PyMOL and then visualised using a Putty model. (<https://github.com/tongalumina/rmsdca/blob/5a5e55ef97170bfbb5c6a66fdb214b76d3887519/rmsdCA.py>).

**Reporting summary.** Further information on research design is available in the Nature Portfolio Reporting Summary linked to this article.

### Data availability

Ras<sub>WT</sub>-GDP- $\text{BeF}_3^-$ , Ras<sub>pY64</sub>-GDP apo, and Ras<sub>pY64</sub>-GDP- $\text{BeF}_3^-$  structures have been deposited in the Protein Data Bank (PDB) with the accession codes 8CNJ (Supplementary Data 1), 8BWG (Supplementary Data 2), and 8CNN (Supplementary Data 3), respectively.

Received: 6 September 2023; Accepted: 11 January 2024;

Published online: 31 January 2024

### References

1. Karnoub, A. E. & Weinberg, R. A. Ras oncogenes: split personalities. *Nat. Rev. Mol. Cell Biol.* **9**, 517–531 (2008).
2. Gasper, R. & Wittinghofer, F. The Ras switch in structural and historical perspective. *Biol. Chem.* **401**, 143–163 (2020).
3. Milburn, M. V. et al. Molecular switch for signal transduction: Structural differences between active and inactive forms of protooncogenic Ras proteins. *Science* **247**, 939–945 (1990).
4. Scheffzek, K., Ahmadian, M. R. & Wittinghofer, A. GTPase-activating proteins: helping hands to complement an active site. *Trends Biochem. Sci.* **23**, 257–262 (1998).
5. Wittinghofer, A. *Ras superfamily small G proteins: biology and mechanisms* (Ed. 1), pp 25–50 (Springer, 2014).



6. Bunda, S. et al. Src promotes GTPase activity of Ras via tyrosine 32 phosphorylation. *Proc. Natl Acad. Sci. USA* **111**, E3785–E3794 (2014).
7. Kano, Y. et al. Tyrosyl phosphorylation of KRAS stalls GTPase cycle via alteration of switch I and II conformation. *Nat. Commun.* **10**, 224 (2019).
8. Bunda, S. et al. Inhibition of SHP2-mediated dephosphorylation of Ras suppresses oncogenesis. *Nat. Commun.* **6**, 8859 (2015).
9. Rezaei Adariani, S. et al. A comprehensive analysis of RAS-effector interactions reveals interaction hotspots and new binding partners. *J. Biol. Chem.* **296**, 100626 (2021).
10. Khaled, M., Gorfe, A. & Sayyed-Ahmad, A. Conformational and dynamical effects of Tyr32 phosphorylation in K-Ras: Molecular dynamics simulation and Markov state models analysis. *J. Phys. Chem. B* **123**, 7667–7675 (2019).
11. Wang, Y. et al. Mechanistic insights into the effect of phosphorylation on Ras conformational dynamics and its interactions with cell signaling proteins. *Comput. Struct. Biotechnol. J.* **19**, 1184–1199 (2021).
12. Ilter, M. et al. Inhibition of mutant RAS-RAF interaction by mimicking structural and dynamic properties of phosphorylated RAS. *Elife* **11**, e79747 (2022).
13. Washington, C. et al. A conserved, N-terminal tyrosine signal directs Ras for inhibition by Rabex-5. *PLoS Genet* **16**, e1008715 (2020).
14. Blackburn, G. M., Kent, D. E. & Kolkman, F. The synthesis and metal binding characteristics of novel, isopolar phosphonate analogues of nucleotides. *J. Chem. Soc., Perkin Trans. 1*, 1119–1125 (1984).
15. Mann, D., Güldenaupt, J., Schartner, J., Gerwert, K. & Köttig, C. The protonation states of GTP and GppNHP in Ras. *proteins J. Biol. Chem.* **293**, 3871–3879 (2018).
16. Knihtila, R., Holzapfel, G., Weiss, K., Meilleur, F. & Mattos, C. Neutron crystal structure of RAS GTPase puts in question the protonation state of the GTP  $\gamma$ -phosphate. *J. Biol. Chem.* **290**, 31025–31036 (2015).
17. Jin, Y., Richards, N. G., Waltho, J. P. & Blackburn, G. M. Metal fluorides as analogues for studies on phosphoryl transfer enzymes. *Angew. Chem. Int. Ed.* **56**, 4110–4128 (2017).
18. Jin, Y., Molt, R. W., Waltho, J. P., Richards, N. G. J. & Blackburn, G. M.  $^{19}\text{F}$ NMR and DFT analysis reveal structural and electronic transition state features for RhoA-catalyzed GTP hydrolysis. *Angew. Chem. Int. Ed.* **55**, 3318–3322 (2016).
19. Jin, Y. et al. Assessing the influence of mutation on GTPase transition states by using X-ray crystallography,  $^{19}\text{F}$ NMR, and DFT approaches. *Angew. Chem. Int. Ed.* **56**, 9732–9735 (2017).
20. Jin, Y. et al. Charge-balanced metal fluoride complexes for Protein Kinase A with adenosine diphosphate and substrate peptide SP20. *Angew. Chem. Int. Ed.* **51**, 12242–12245 (2012).
21. Cliff, M. J. et al. Transition state analogue structures of human phosphoglycerate kinase establish the importance of charge balance in catalysis. *J. Am. Chem. Soc.* **132**, 6507–6516 (2010).
22. Baxter, N. J. et al.  $\text{MgF}_3^-$  and alpha-galactose 1-phosphate in the active site of beta-phosphoglucomutase form a transition state analogue of phosphoryl transfer. *J. Am. Chem. Soc.* **131**, 16334–16335 (2009).
23. Baxter, N. J. et al. Atomic details of near-transition state conformers for enzyme phosphoryl transfer revealed by  $\text{MgF}_3^-$  rather than by phosphoranes. *Proc. Natl Acad. Sci. USA* **107**, 4555–4560 (2010).
24. Forget, S. M. et al. Synthesis and enzymatic evaluation of ketose phosphonates: the interplay between mutarotation, monofluorination and acidity. *Chem. Sci.* **3**, 1866–1878 (2012).
25. Griffin, J. L. et al. Near attack conformers dominate  $\beta$ -phosphoglucomutase complexes where geometry and charge distribution reflect those of substrate. *Proc. Natl Acad. Sci. USA* **109**, 6910–6915 (2012).
26. Johnson, L. A. et al. Van der Waals contact between nucleophile and transferring phosphorus is insufficient to achieve enzyme transition-state architecture. *ACS Catal.* **8**, 8140–8153 (2018).
27. Robertson, A. J. et al. The relationship between enzyme conformational change, proton transfer, and phosphoryl transfer in  $\beta$ -phosphoglucomutase. *ACS Catal.* **11**, 12840–12849 (2021).
28. Liu, Y. et al. A pH-gated conformational switch regulates the phosphatase activity of bifunctional HisKA-family histidine kinases. *Nat. Commun.* **8**, 2104 (2017).
29. Greiner, J. V. & Glonek, T. Intracellular ATP concentration and implication for cellular evolution. *Biology* **10**, 1166 (2021).
30. Blackburn, G. M. et al. How to name atoms in phosphates, polyphosphates, their derivatives and mimics, and transition state analogues for enzyme-catalysed phosphoryl transfer reactions (IUPAC Recommendations 2016). *Pure Appl. Chem.* **89**, 653–675 (2017).
31. Geyer, M. et al. Conformational transitions in p21ras and in its complexes with the effector protein Raf-RBD and the GTPase activating protein GAP. *Biochemistry* **35**, 10308–10320 (1996).
32. Molt, R. W. Jr, Pellegrini, E. & Jin, Y. A GAP-GTPase-GDP-Pi intermediate crystal structure analyzed by DFT shows GTP hydrolysis involves serial proton transfers. *Chemistry* **25**, 8484–8488 (2019).
33. Scheidig, A. J., Burmester, C. & Goody, R. S. The pre-hydrolysis state of p21(ras) in complex with GTP: new insights into the role of water molecules in the GTP hydrolysis reaction of ras-like proteins. *Structure* **7**, 1311–1324 (1999).
34. Åqvist, J. & Kamerlin, S. C. L. Conserved motifs in different classes of GTPases dictate their specific modes of catalysis. *ACS Catal.* **6**, 1737–1743 (2016).
35. Nemukhin, A. V., Grigorenko, B. L. & Shadrina, M. S. Mechanisms of enzymatic hydrolysis of nucleoside triphosphates by quantum and molecular mechanics. *Russ. J. Gen. Chem.* **78**, 696–703 (2008).
36. Menyhard, D. K. et al. Structural impact of GTP binding on downstream KRAS signaling. *Chem. Sci.* **11**, 9272–9289 (2020).
37. Novelli, E. T., First, J. T. & Webb, L. J. Quantitative measurement of intrinsic GTP hydrolysis for carcinogenic glutamine 61 mutants in H-Ras. *Biochemistry* **57**, 6356–6366 (2018).
38. Langen, R., Schweins, T. & Warshel, A. On the mechanism of guanosine triphosphate hydrolysis in ras p21 proteins. *Biochemistry* **31**, 8691–8696 (1992).
39. Klähn, M., Rosta, E. & Warshel, A. On the mechanism of hydrolysis of phosphate monoesters dianions in solutions and proteins. *J. Am. Chem. Soc.* **128**, 15310–15323 (2006).
40. Carvalho, A. T. P., Szeler, K., Vavitsas, K., Åqvist, J. & Kamerlin, S. C. L. Modeling the mechanisms of biological GTP hydrolysis. *Arch. Biochem. Biophys.* **582**, 80–90 (2015).
41. Danielson, M. A. & Falke, J. J. Use of  $^{19}\text{F}$  NMR to probe protein structure and conformational changes. *Annu. Rev. Biophys. Biomol. Struct.* **25**, 163–195 (1996).
42. Hansen, P. E., Dettman, H. D. & Sykes, B. D. Solvent-induced deuterium isotope effects on  $^{19}\text{F}$  chemical shifts of some substituted fluorobenzenes. Formation of inclusion complexes. *J. Magn. Reson.* **62**, 487–496 (1985).
43. Scheffzek, K. et al. The Ras-RasGAP complex: structural basis for GTPase activation and its loss in oncogenic Ras mutants. *Science* **277**, 333–338 (1997).
44. Simão, S., Agostinho, R. R., Martínez-Ruiz, A. & Araújo, I. M. Regulation of Ras signaling by S-nitrosylation. *Antioxidants* **12**, 1562 (2023).
45. Seeliger, M. A. et al. High yield bacterial expression of active c-Abl and c-Src tyrosine kinases. *Prot. Sci.* **14**, 3135–3139 (2005).
46. Rosenau, C. P., Jelier, B. J., Gossert, A. D. & Togni, A. Exposing the origins of irreproducibility in fluorine NMR spectroscopy. *Angew. Chem. Int. Ed.* **57**, 9528–9533 (2018).
47. D’Arcy, A., Bergfors, T., Cowan-Jacob, S. W. & Marsh, M. Microseed matrix screening for optimization in protein crystallization: what have we learned? *Acta Crystallogr. F. Struct. Biol. Commun.* **70**, 1117–1126 (2014).
48. Kabsch, W. Xds. *Acta Crystallogr. D. Biol. Crystallogr.* **66**, 125–132 (2010).
49. Evans, P. Scaling and assessment of data quality. *Acta Crystallogr. D. Biol. Crystallogr.* **62**, 72–82 (2006).
50. Winter, G. xia2: An expert system for macromolecular crystallography data reduction. *J. Appl. Crystallogr.* **43**, 186–190 (2009).
51. Lebedev, A. A., Vagin, A. A. & Murshudov, G. N. Model preparation in MOLREP and examples of model improvement using X-ray data. *Acta Crystallogr. D. Biol. Crystallogr.* **64**, 33–39 (2008).
52. Murshudov, G. N., Vagin, A. A. & Dodson, E. J. Refinement of macromolecular structures by the maximum-likelihood method. *Acta Crystallogr. D. Biol. Crystallogr.* **53**, 240–255 (1997).

## Acknowledgements

We thank Dr. Pierre Rizkallah from Cardiff University Medical School and Dr. Colin Levy from the University of Manchester for assistance with the x-ray data collection, and the Diamond Light Source for access to beamline I03 under proposal numbers mx31850 and mx20147. We thank Dr. Matt Cliff from the University of Manchester for assistance with NMR. We thank Prof. G. Mike Blackburn for critical discussions. We are indebted to the Wellcome Trust Seed Award (209057/Z/17/Z) and The Academy of Medical Sciences Springboard Award (SBE003\1154) for supporting P.B. and Y.J., who is a Wellcome Trust Sir Henry Dale Fellow (218568/Z/19/Z).

## Author contributions

P.B. performed cloning, mutagenesis, gene expression, protein production, phosphorylation assay,  $^{31}\text{P}$  and  $^{19}\text{F}$  NMR, protein crystallography and data refinement. Y.J. performed protein crystallography, data refinement, and supervised the studies. P.B. and Y.J. wrote the manuscript.

**Competing interests**

The authors declare no competing interests.

**Additional information**

**Supplementary information** The online version contains supplementary material available at <https://doi.org/10.1038/s42004-024-01105-6>.

**Correspondence** and requests for materials should be addressed to Yi Jin.

**Peer review information** *Communications Chemistry* thanks Helen Mott and the other anonymous reviewers for their contribution to the peer review of this work.

**Reprints and permission information** is available at <http://www.nature.com/reprints>

**Publisher's note** Springer Nature remains neutral with regard to jurisdictional claims in published maps and institutional affiliations.



**Open Access** This article is licensed under a Creative Commons Attribution 4.0 International License, which permits use, sharing, adaptation, distribution and reproduction in any medium or format, as long as you give appropriate credit to the original author(s) and the source, provide a link to the Creative Commons licence, and indicate if changes were made. The images or other third party material in this article are included in the article's Creative Commons licence, unless indicated otherwise in a credit line to the material. If material is not included in the article's Creative Commons licence and your intended use is not permitted by statutory regulation or exceeds the permitted use, you will need to obtain permission directly from the copyright holder. To view a copy of this licence, visit <http://creativecommons.org/licenses/by/4.0/>.

© The Author(s) 2024